

Multimaterial Additively Manufactured Transmissive Spin-Decoupled Polarization-Maintaining Metasurfaces

Jianfeng Zhu, Mengze Li, Jiexin Lai, and Yang Yang*

Taking advantage of multimaterial additive manufacturing, this work demonstrates a kind of polarization-maintaining metasurface (MS) for spin-decoupled beam shaping. The wavefronts of the two spin states, i.e., the left-hand circular polarization (LHCP) and the right-hand circular polarization (RHCP), can be independently manipulated while the output spin state remains the same as the input. The meta-atom is implemented with dual-polarized antennas at the top and the bottom with phase delay lines connecting them. The dual-polarized antenna on the receiving side is fixed to receive the LHCP/RHCP incident waves, while the dual-polarized transmitting antenna is rotated, providing the opposite phase shifts for the LHCP and RHCP. The absolute value of the phase shift is the same as the transmitting antenna's rotation angle. Meanwhile, varying the length of phase delay lines introduces 2π phase shifts for both LHCP and RHCP inputs. Thus, combining the two phase-shifting degrees of freedom, the LHCP and RHCP wavefronts can be independently controlled while the polarization is not flipped after transmitting through the MS. One MS produces vortex beams with different topological charges for LHCP and RHCP. The other achieves spin-decoupled focusing. The multilayered MSs are conveniently printed using multimaterial additive manufacturing without postprocessing.

light-matter interaction to produce abrupt phase changes, which are superior to conventional optical materials where phase accumulation generally depends on wave propagation over long distances.^[16] One common method is introducing local phase modulations with unaffected amplitude to achieve efficient wavefront control. For instance, Pancharatnam–Berry (P–B) phase is one approach to manipulating the phase of the circularly polarized wave.^[17–20] The phase shifting is achieved by rotating the anisotropic meta-atom. The phase shifts show an opposite tendency for the two spin states, with the phase-shift values twice the rotation angle. Nevertheless, this symmetric feature has limited the P–B phase to wider applications. The issue is recently solved by adding dynamic phase into the P–B phase.^[21–35] Versatile devices with left-hand circular polarization (LHCP) and right-hand circular polarization (RHCP) fully decoupled features are demonstrated. For example, spin-controlled MS was demonstrated


1. Introduction

Metasurfaces (MSs), which usually consist of 2D arrays of sub-wavelength meta-atoms with spatially varying geometric parameters, have drawn considerable research interest over the last decades.^[1–15] MSs manipulate the waves by introducing strong

for spin angular momentum (SAM) and orbital angular momentum (OAM) sorting, paving the way to highly integrated optical and quantum systems.^[36] High-efficiency bilayer spin-decoupled information MSs were realized to achieve polarization-encoded holograms.^[37] Multiple wavelength spin-decoupled MSs were demonstrated with frequency and polarization multiplexing, supporting high-speed wireless communication systems.^[26,29] Unlike the strategy of the joint modulation of the geometric phase and dynamic phase, the pure geometric phase was also demonstrated to design meta-lens with spin-decoupled imaging,^[38] vortex beams,^[27] and intensity-tunable focusing.^[39] Nevertheless, because of the inherent nature of the P–B phase, the spin always flips after transmitting through these MSs. In practical scenarios such as satellite communications, spin states must be maintained at transmitting and receiving ends when transmitting and receiving data. Therefore, exploring an efficient phase-modulation mechanism for maintaining circular polarization and independent wavefront shaping is necessary, avoiding using an additional polarization conversion layer atop the traditional spin-decoupled MS.^[40] Recently, chirality-assisted P–B phase MS was demonstrated to independently manipulate the co-polarization and cross-polarization of the LHCP/RHCP channels.^[41] However, the amplitude responses cannot be controlled, and the efficiency is partly sacrificed.

J. Zhu
School of Electronic and Information Engineering
South China University of Technology
Guangzhou 510642, China

J. Zhu, M. Li, J. Lai, Y. Yang
School of Electrical and Data Engineering
University of Technology Sydney
Tech Lab, NSW 2019, Australia
E-mail: yang.yang-1@uts.edu.au

 The ORCID identification number(s) for the author(s) of this article can be found under <https://doi.org/10.1002/lpor.202300433>

© 2023 The Authors. Laser & Photonics Reviews published by Wiley-VCH GmbH. This is an open access article under the terms of the Creative Commons Attribution-NonCommercial-NoDerivs License, which permits use and distribution in any medium, provided the original work is properly cited, the use is non-commercial and no modifications or adaptations are made.

DOI: 10.1002/lpor.202300433

Circular polarization-decoupled MS was demonstrated using antenna-transmission line-antenna type meta-atoms.^[42] Although the geometric phase shifting is different from the P–B phase, the MS only decouples the LHCP and RHCP components under a specific linear polarization wave illumination. Hence, the MS can only be regarded as a degenerated case of the conventional spin-decoupled MSs. To the author’s knowledge, spin-decoupled MSs with a circular polarization-maintaining feature are rarely reported.

This article demonstrates a kind of polarization-maintaining MS for spin-decoupled beam shaping. The wavefront of the two spin states, i.e., the LHCP and RHCP, can be independently manipulated while the output spin state remains the same as that of the input. On the receiving side of the meta-atom, the dual-polarized antenna receives the LHCP/RHCP incident waves and converts them into guided mode along the phase delay lines. Then, the energy along the phase delay lines is smoothly induced into the dual-polarized antenna on the transmitting side and radiated into free space. The dual-polarized antenna on the receiving side is fixed. In contrast, the dual-polarized antenna on the transmitting side rotates, providing the opposite phase shifts for the LHCP and RHCP. The absolute value of the phase shifts is equal to the transmitting antenna’s rotation angle. Meanwhile, adjusting the length of phase delay lines introduces 2π phase shifts for both LHCP and RHCP incident waves. Thus, by combining the two phase-shifting degrees of freedom, the LHCP and RHCP wavefront can be independently controlled. At the same time, the polarization is not flipped after transmitting through the MS. In addition, the MS maintains a small lateral size and can be conveniently fabricated using multimaterial additive manufacturing without postprocessing. For proof of concept, two spin-decoupled polarization-maintaining MSs with different functions are designed and experimentally verified. One MS produces vortex beams with different topological charges for two spin states, while the other achieves spin decoupled focusing on predefined positions.

2. Experimental Section

The MSs were printed using the multimaterial-integrated additive manufacturing technique. Two heads, with each head consisting of 512 piezoelectric-based nozzles, were simultaneously used during the printing. One head was connected to a silver nanoparticle ink-filled chamber for conductor printing. The other was connected to the chamber filled with UV-curable acrylate ink for dielectric printing, as illustrated in **Figure 1a**. An ultrathin soldering mask layer was printed first above the platform. Then, the predesigned patterns could be built on it. The thickness of the metal layers could be flexibly designed. A thickness of 0.035 mm was chosen to provide a robust connection while maintaining a thin thickness. During printing, a near-infrared radiation (NIR) lamp (0.75–1.4 μm) and a UV lamp (395 nm) were used to sinter conductor ink and dielectric ink, respectively. The prototype was printed layer by layer. An additional ultrathin solder mask was printed on the top when printing the predesigned patterns was finished. The low-temperature additive manufacturing steps are shown in **Figure 1b**. The MS samples were measured in a near-field measurement setup. The LHCP and RHCP horn antennas were, respectively, used to feed the MS, and the LHCP

and RHCP probes were arranged in 50 mm to the MS’s aperture and scanned in the 2D plane to receive the power and phase.

3. Principle and Design

The schematic function of the spin-decoupled polarization-maintaining MS is illustrated in **Figure 2**. Vortex beams with different topological charges can be realized under LHCP and RHCP illuminations, respectively. Meanwhile, the output spin state is the same as the input. The basic configuration and dimensions of the meta-atom are shown in **Figure 3**. Dual-polarized patch antennas are arranged on the top and bottom of the meta-atom with phase delay lines connecting them in between. The phase delay lines are folded so that the meta-atom can maintain a small lateral size. All the conductor layers are made of silver nanoparticle ink. In the meantime, ultraviolet (UV) curable acrylate ink (a dielectric constant of 2.8 and a loss tangent of 0.012) is printed as a dielectric layer to hold multiple conductor layers. Without loss of generality, considering the LHCP ($|L\rangle = [1, j]/\sqrt{2}$) as the input, it can be directly received by the dual-polarized antenna and then converted to the guided mode along the phase delay line. Thus, the Jones vector of E -field can be written as

$$E = \begin{bmatrix} e^{-j\varphi} & 0 \\ 0 & e^{-j\varphi} \end{bmatrix} \cdot \frac{\sqrt{2}}{2} \cdot \begin{bmatrix} 1 \\ i \end{bmatrix} \quad (1)$$

where φ is the phase shift because of the phase delay line. The dual-polarized antenna on the transmitting side rotates at an angle of θ . Then, the corresponding E -field of the output can be written as

$$E^{\text{out}} = \begin{bmatrix} \cos \theta & \sin \theta \\ -\sin \theta & \cos \theta \end{bmatrix} \cdot E = \begin{bmatrix} \cos \theta & \sin \theta \\ -\sin \theta & \cos \theta \end{bmatrix} \cdot \begin{bmatrix} e^{-j\varphi} & 0 \\ 0 & e^{-j\varphi} \end{bmatrix} \cdot \frac{\sqrt{2}}{2} \cdot \begin{bmatrix} 1 \\ i \end{bmatrix} = e^{-j\varphi} \cdot e^{j\theta} \cdot \frac{\sqrt{2}}{2} \cdot \begin{bmatrix} 1 \\ i \end{bmatrix} \quad (2)$$

Similarly, considering the RHCP ($|R\rangle = [1, -j]/\sqrt{2}$) as the input, the output E -field can be written as

$$E^{\text{out}} = \begin{bmatrix} \cos \theta & \sin \theta \\ -\sin \theta & \cos \theta \end{bmatrix} \cdot \begin{bmatrix} e^{-j\varphi} & 0 \\ 0 & e^{-j\varphi} \end{bmatrix} \cdot \frac{\sqrt{2}}{2} \cdot \begin{bmatrix} 1 \\ -i \end{bmatrix} = e^{-j\varphi} \cdot e^{-j\theta} \cdot \frac{\sqrt{2}}{2} \cdot \begin{bmatrix} 1 \\ -i \end{bmatrix} \quad (3)$$

It can be seen from Equations (2) and (3) that rotating the transmitting antenna provides opposite phase delays for the LHCP and RHCP incidence. The absolute phase-shift values are equal to the rotation angle θ . Besides, varying the length of the phase delay line offers the same phase shifts for both LHCP and RHCP inputs. Then, by combining the two uncorrelated phase shifting degrees of freedom, the LHCP and RHCP waves can be fully decoupled. More importantly, in contrast to the P–B phase-based spin-decoupled strategy, where the spin flips after transmitting through the MS, the output spin state remains the same as that of the input, as seen from Equations (2) and (3).

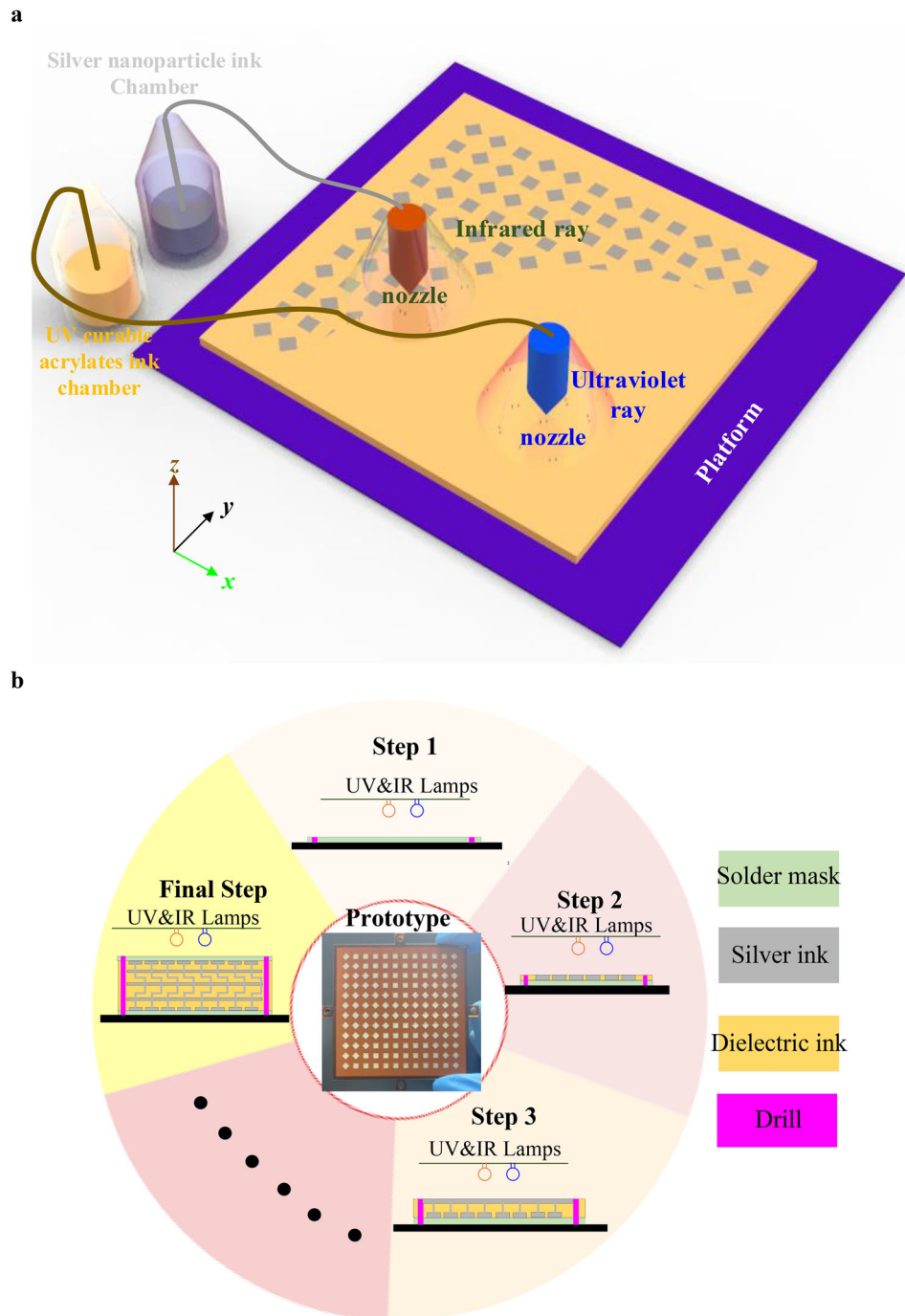


Figure 1. a) The MS under manufacturing. b) Steps of the multimaterial additive manufacturing.

Here, the challenge for the MS implementation lies in the fact that the position and the topology of the phase delay line are related to the transmitting antenna's rotation angle (including its feed probe). In other words, when the transmitting antenna rotates, the position, length, and topology of the phase delay line must be changed correspondingly to ensure high transmission magnitude and accurate dynamic phase delay. Ideally, we must find a set of proper phase delay lines for each rotation angle θ . Here, the rotation angle of the transmitting antenna is quantized

into eight types to ease the design, namely, 0° (marked as type A), 45° (type B), 90° (type C), 135° (type D), 180° (type E), 225° (type F), 270° (type G), and 315° (type H). Then, a set of phase delay lines is carefully selected to provide 2π dynamic phase shifting for types A–H. The dynamic phase shifts are realized by adjusting the length of phase delay lines.

Since the phase delay lines are planar configurations, they can be bent when the length of the phase delay lines increases. Fortunately, the real estate of the unit cell is enough to support

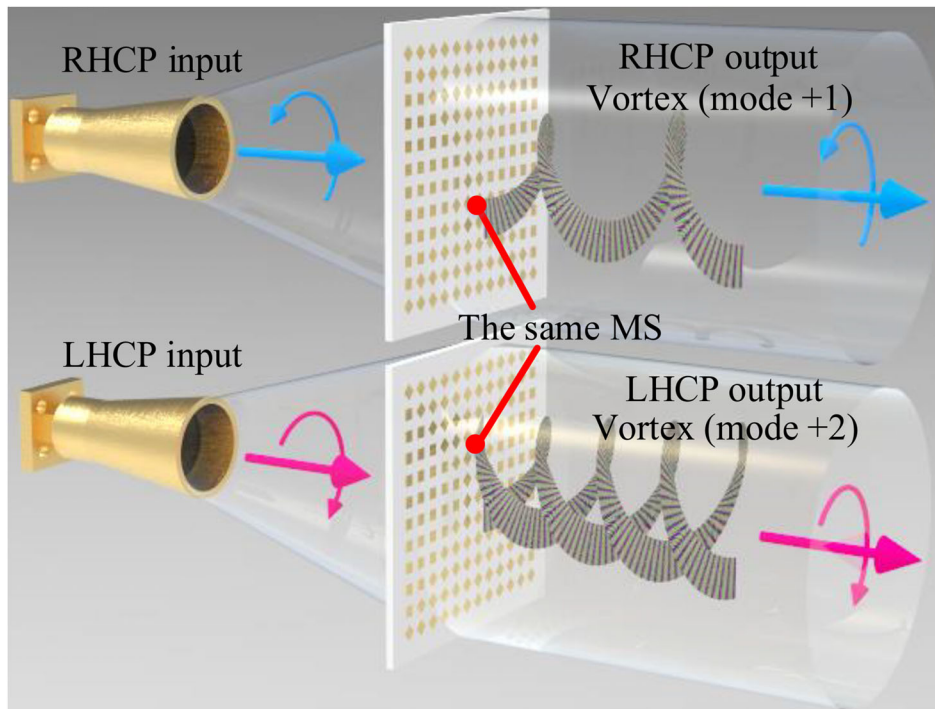


Figure 2. Schematic of the additively manufactured spin-decoupled polarization-maintaining MS. Vortex beams with different topological charges can be achieved under LHCP and RHCP illuminations. The output polarization is the same as that of the input.

different phase delay line lengths covering 2π phase shifting. If the space is insufficient to support the phase delay lines, we can add more layers to provide adequate space, making all the unit cells the same height to avoid the MS being nonplanar. Eight-level meta-atoms (marked as I to VIII) are selected to cover the 2π

dynamic phase with a step of 45° for types A–H. In other words, 64 meta-atoms are adopted to form the MS. A schematic view of the 64 meta-atoms' phase-shift map is presented in **Figure 4a**. Along the horizontal axis (from type A to type H), the phase shift comes from the transmitting antenna's rotation. As an

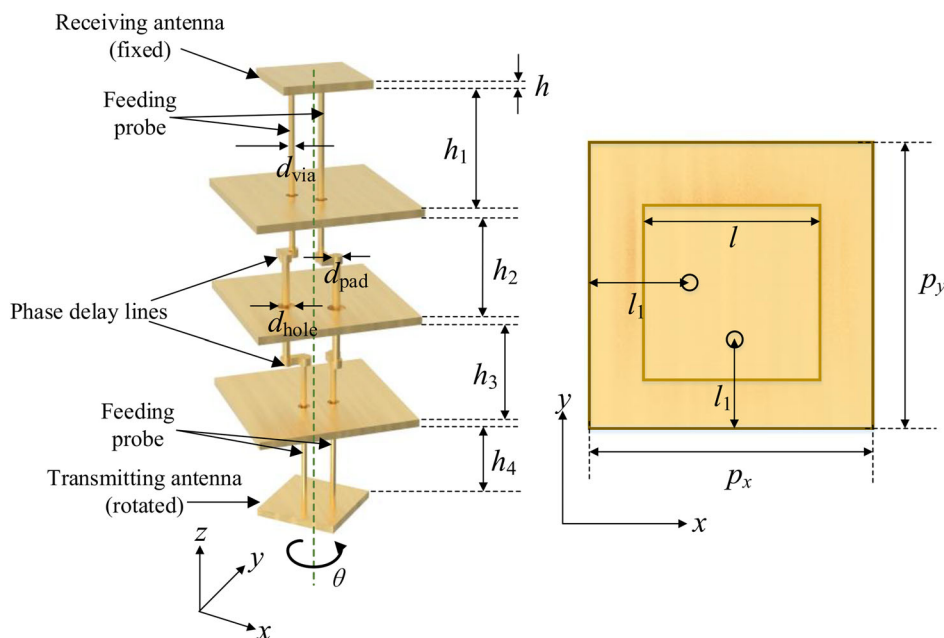
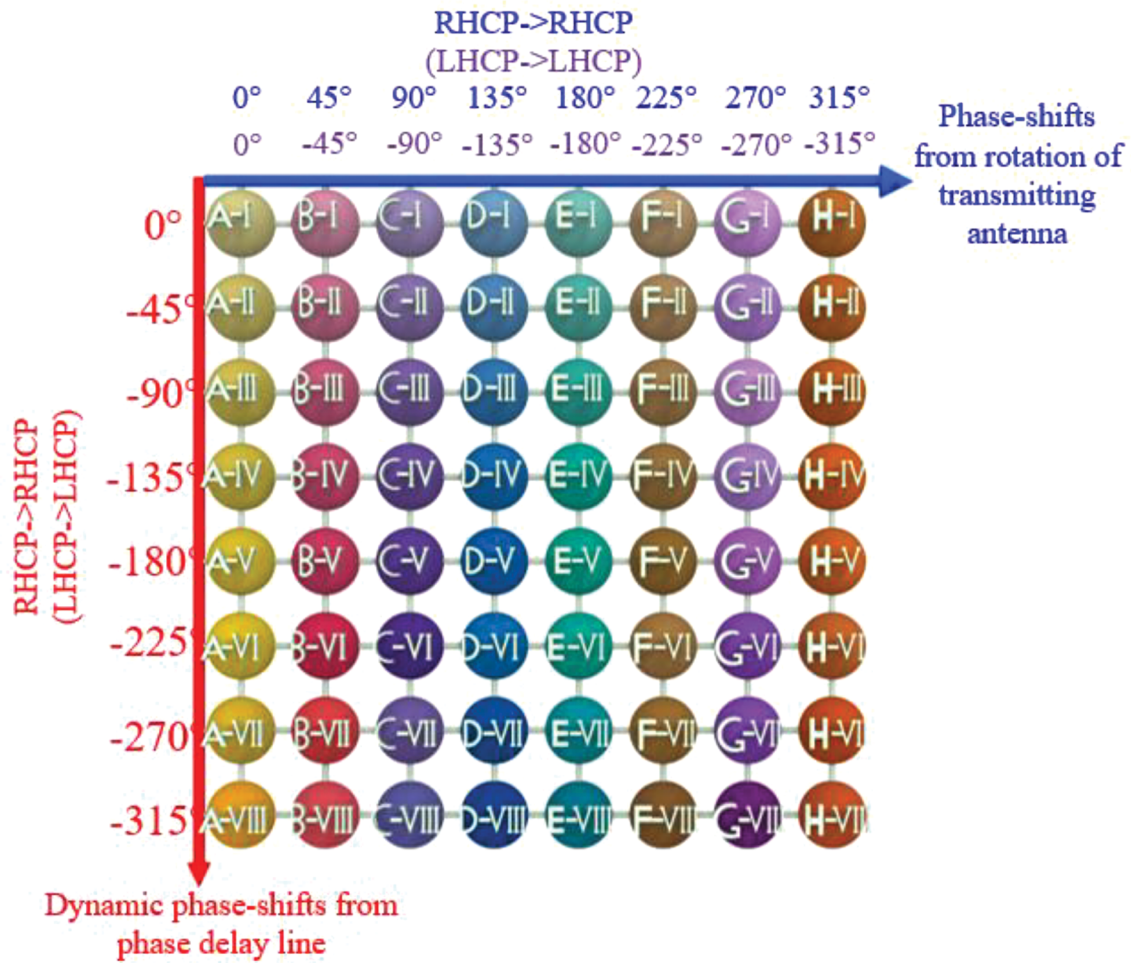


Figure 3. Geometry of the meta-atom (not scaled in the z-direction). $h_1 = 0.035$ mm, $h_2 = 0.47$ mm, $h_3 = 0.435$ mm, $h_4 = 0.435$ mm, $h_5 = 0.47$ mm, $p_x = 5.4$ mm, $p_y = 5.4$ mm, $d_{\text{via}} = 0.2$ mm, $d_{\text{hole}} = 0.4$ mm, $d_{\text{pad}} = 0.4$ mm $l = 2.8$ mm, and $l_1 = 1.97$ mm.

a



b

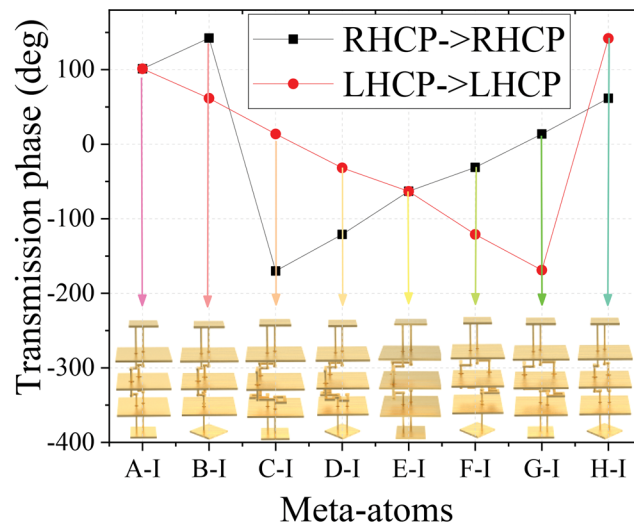


Figure 4. a) Schematic view of the phase distribution of the 64 meta-atoms. b) Co-polarization transmission phase of the meta-atoms from A-I to H-I. For type E-I, the phase delay line is enlarged to provide additional 180° phase shifts compared with type A-I, equal to the transmitting antenna rotated at an angle of 180° compared with type A-I.

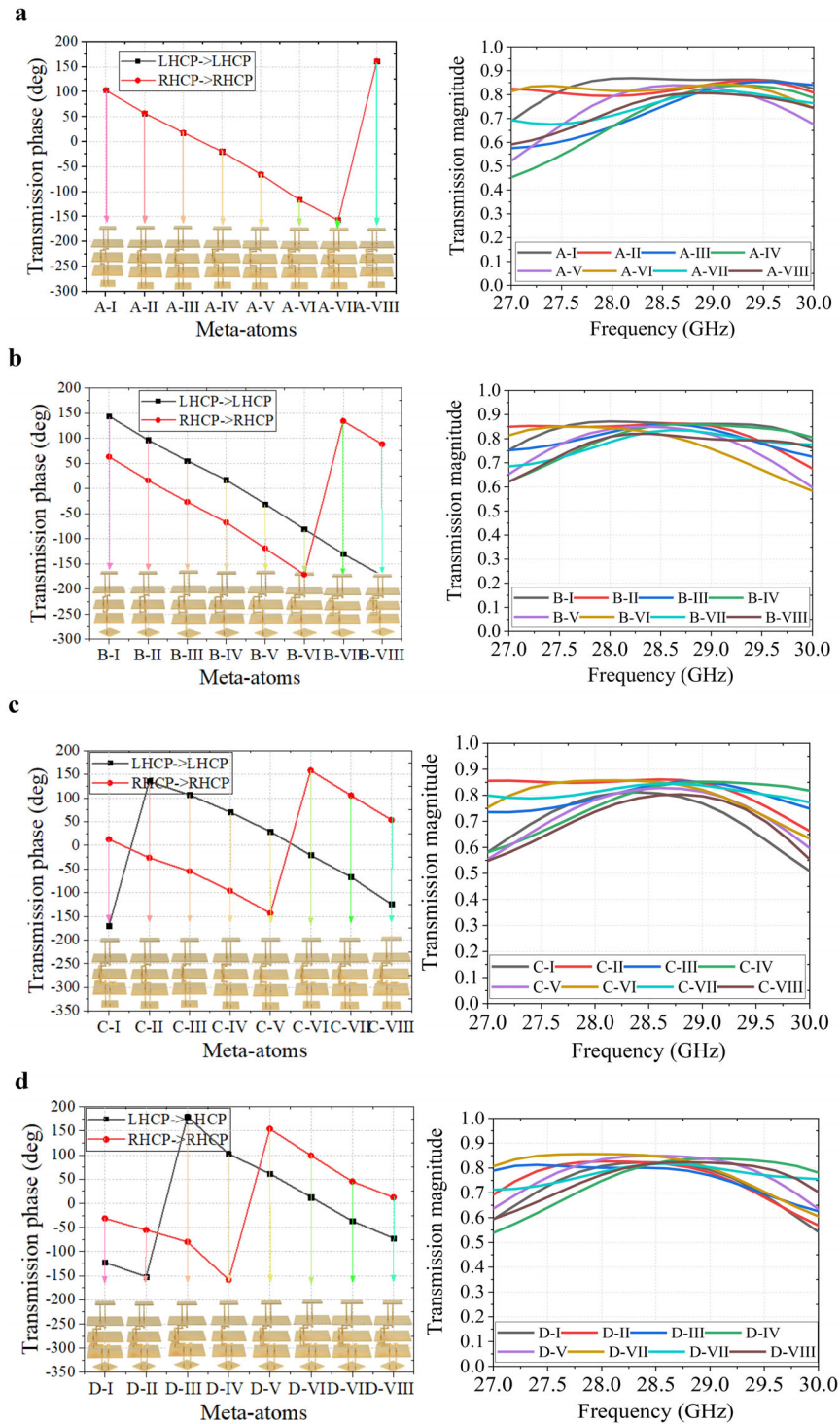


Figure 5. Transmission phase and magnitude of different types of meta-atoms. a) Type A. b) Type B. c) Type C. d) Type D.

example, the co-polarization transmission phase of the meta-atoms in the first row (from A-I to H-I) is given in Figure 4b. It is observed that the phase shift of the LHCP and RHCP shows opposite tendencies, and the phase shift is around 45° a step. Along the vertical axis (from I to VIII), the dynamic phase shift is introduced by varying the length of phase delay line of meta-atoms,

and the phase shifts are the same for both LHCP and RHCP inputs.

The configuration of the meta-atoms with different dynamic phase shifts for types A–D and their corresponding co-polarization transmission phase and magnitude are shown in **Figure 5**. The configuration of the meta-atoms for types E–H

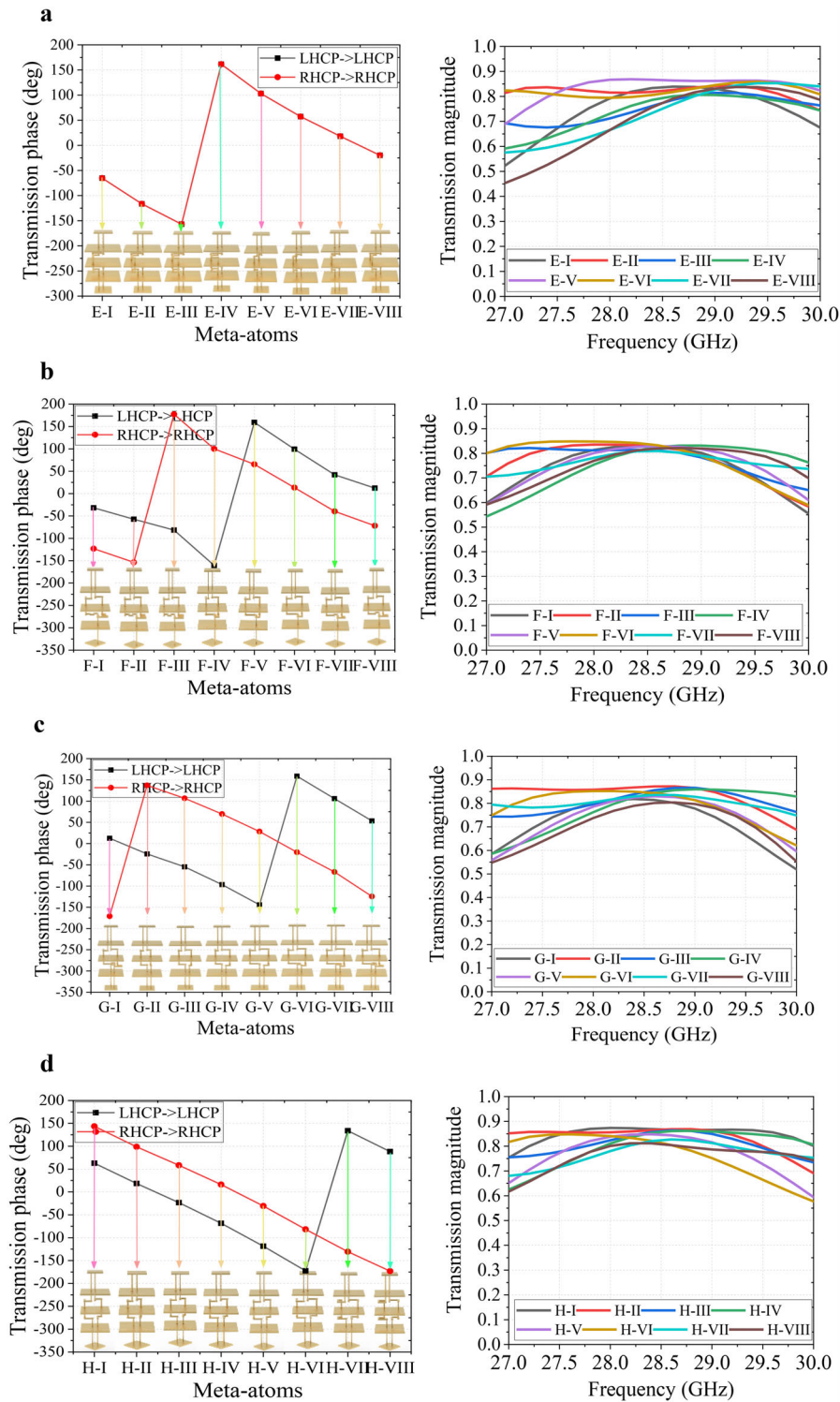


Figure 6. Transmission phase and magnitude of different type of meta-atoms. a) Type E. b) Type F. c) Type G. d) Type H.

and their corresponding co-polarization transmission phase and magnitude are given in **Figure 6**. The length of phase delay lines and the topology of each meta-atom are carefully optimized in Ansys HFSS by using the pattern-search-based algorithm to match the required phase shift and achieve a high transmission

magnitude. As can be observed, adjusting the length of phase delay line offers the same phase shifts for the LHCP and RHCP. The phase shifts are around 45° a step from I to VIII. The transmission magnitudes of the meta-atoms are between 0.7 and 0.9 in most of the band. Because the UV-curable acrylate ink is lossy,

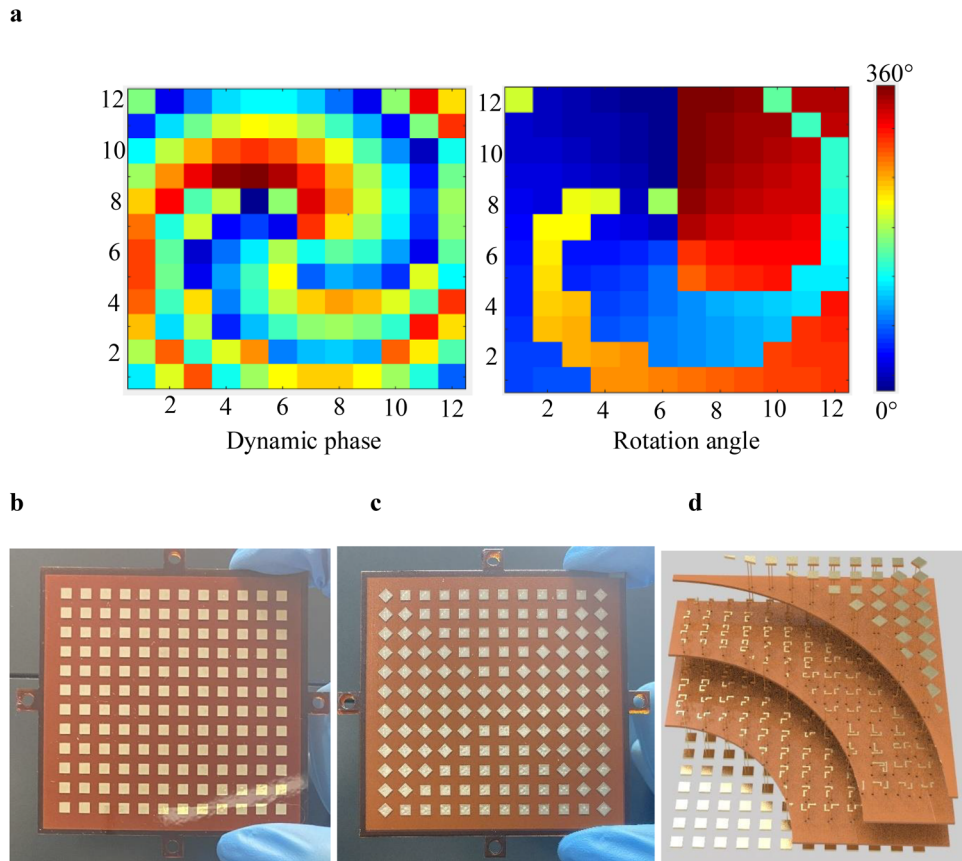


Figure 7. a) Dynamic phase shifts of each meta-atom, and the rotation angle (α) of the dual-polarized antenna in the transmitting side on the MS's aperture. b) Top view of the MS sample. c) Bottom view of the MS sample. d) Internal view.

some of the energy is dissipated in the dielectric material. If there is no loss from the UV-curable acrylate ink, the transmission magnitude can be improved by 0.1 on average. More detailed dimensions of the 64 meta-atoms are provided in Figure S1 (Supporting Information).

4. Results

The MS must provide two uncorrelated phase profiles for the two spin states, i.e., $\delta_L(x, y)$ for LHCP and $\delta_R(x, y)$ for RHCP. Based on Equations (2) and (3), the required dynamic phase (Γ) from the phase delay line can be expressed as

$$\Gamma(x, y) = \frac{1}{2}(\delta_L(x, y) + \delta_R(x, y)) \quad (4)$$

Meanwhile, the rotation angle (α) of the dual-polarized antenna on the transmitting side can be calculated as

$$\alpha(x, y) = \frac{1}{2}(\delta_L(x, y) - \delta_R(x, y)) \quad (5)$$

For verification, two spin-decoupled polarization-maintaining MSs are designed with different functionalities. The first MS (MS I) collimates the electromagnetic wave and generates vortex beams with different topological charges for LHCP (topological

charge $l = 2$) and RHCP (topological charge $l = 1$). Therefore, the required phase profile of the MS for LHCP and RHCP can be, respectively, expressed as

$$\delta_L(x, y) = (\sqrt{x^2 + y^2 + F^2} - F)k_0 + 2 \cdot \varphi \text{ for LHCP} \quad (6)$$

$$\delta_R(x, y) = (\sqrt{x^2 + y^2 + F^2} - F)k_0 + \varphi \text{ for RHCP} \quad (7)$$

where F is the focal length, k_0 is the free-space wavenumber. Combining Equations (4)–(7), the dynamic phase shifts of the meta-atom as well as the rotation angle (α) of the dual-polarized antenna on the transmitting side can be obtained, as shown in Figure 7a. Then, the corresponding meta-atoms in Section 2 can be selected to be arranged on the MS's aperture. The MS is fast prototyped using the multimaterial additive manufacturing technique. The top and bottom views of the prototype are shown in Figure 7b and Figure 7c, respectively. The internal view of the MS sample is shown in Figure 7d to better reveal the configuration of the phase delay lines between the top and bottom dual-polarized antennas. The performance of the MS is measured in a near-field measurement system. The near-field co-polarization transmission magnitude and phase under LHCP and RHCP wave illuminations at 27.38, 28.77, 29.69, and 30.62 GHz are given in Figure 8a and Figure 8b, respectively. The measured results agree well with the numerical ones. Under LHCP illumination, vortex beams with a topological charge of 2 can be clearly observed from

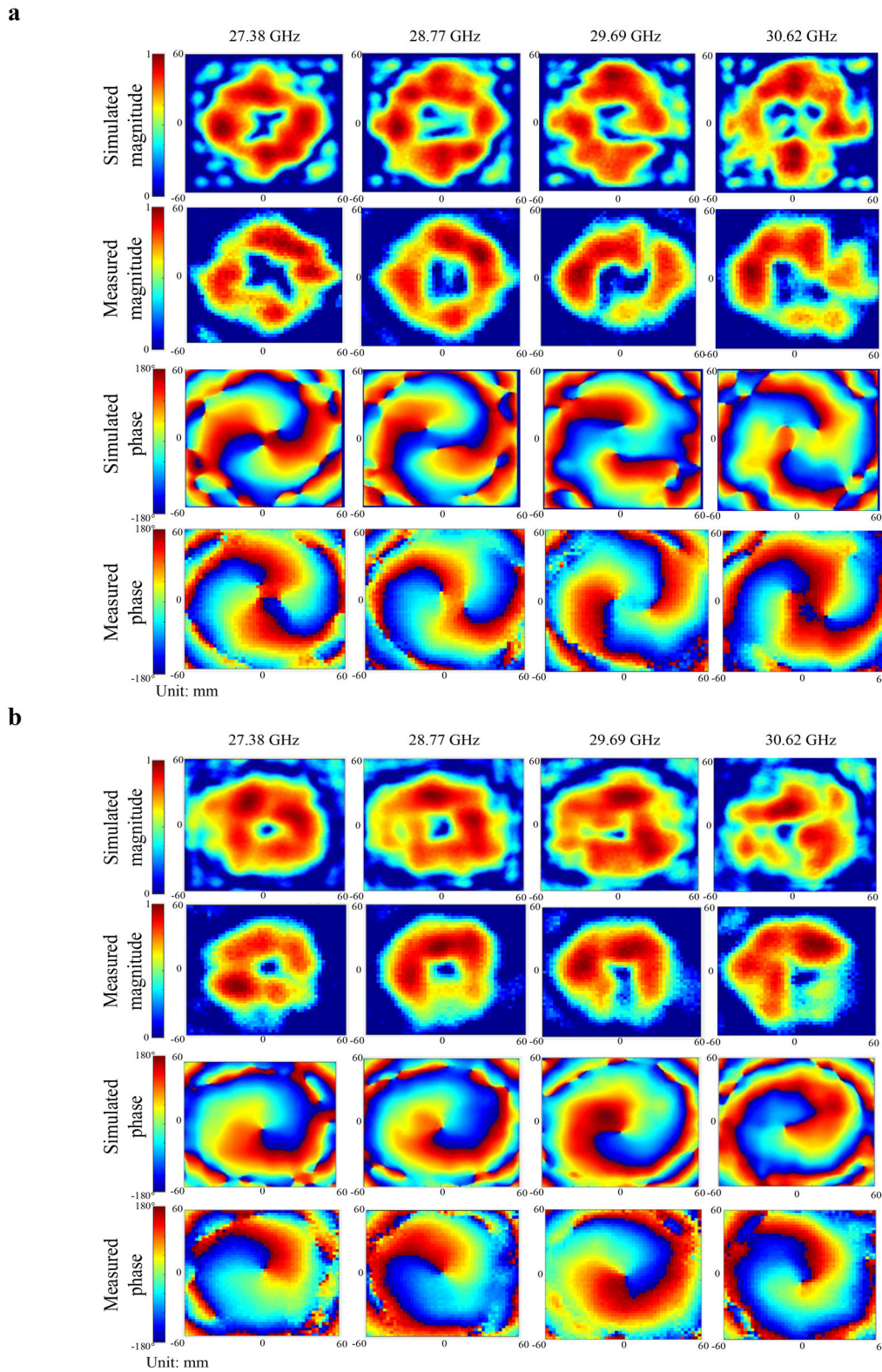


Figure 8. a) Simulated and measured co-polarization transmission magnitude and phase under LHCP illumination (topological charge of 2). b) Simulated and measured co-polarization transmission magnitude and phase under RHCP illumination (topological charge of 1).

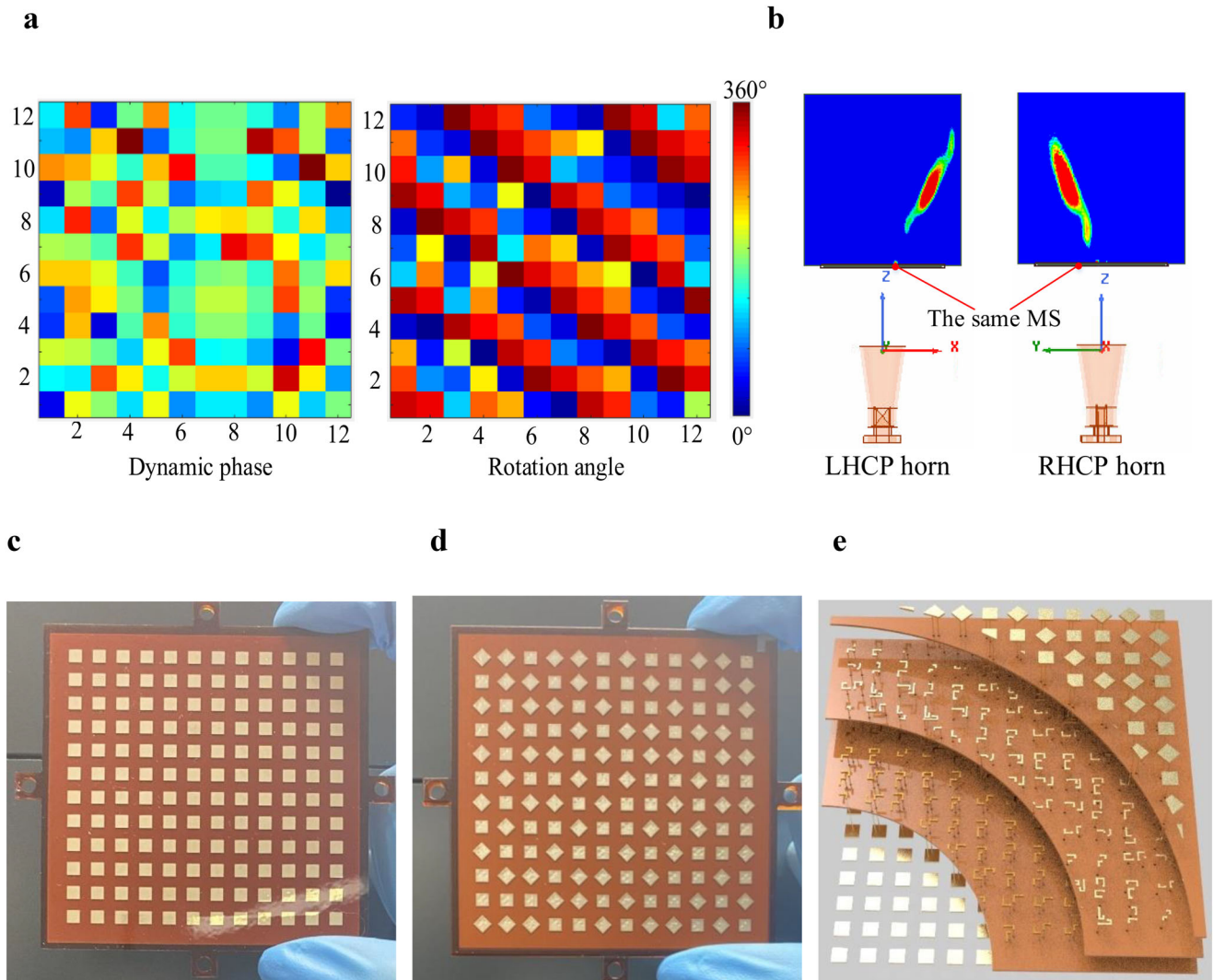


Figure 9. a) Dynamic phase shifts of each meta-atom, and the rotation angle (α) of the dual-polarized antenna in the transmitting side on the MS II's aperture. b) Simulated complex magnitude of the E -field distributions under LHCP (xoz -plane) and RHCP (yoz -plane) illuminations. c) Top view of the MS sample. d) Bottom view of the MS sample. e) Internal view.

the phase profiles of Figure 8a. Under RHCP illumination, vortex beams with the topological charge of 1 can be clearly observed from the phase profiles of Figure 8b. The donut-like profile can be observed in the LHCP and RHCP illumination intensity profiles. Note that the rotating angle of the transmitting antenna and the dynamic phase, i.e., the length of the phase delay line, are both discretized into eight levels covering 2π phase shifting to reduce design complexity; the performance of the vortex is compromised a little bit. The measured intensity and phase profiles of other frequencies are provided in Videos SV1 and SV2 (Supporting Information).

The second MS (MS II) collimates the electromagnetic wave from the source and focuses the LHCP and RHCP waves into different positions. The focusing position is designed to locate at ($x = -30$ mm, $y = 0$ mm, and $z = 50$ mm) for LHCP and ($x = 0$ mm, $y = 20$ mm, and $z = 50$ mm) for RHCP above the MS. **Figure 9a** shows the calculated dynamic phase shifts of each meta-atom and the rotation angle (α) of the dual-polarized antenna in the trans-

mitting side on the MS II's aperture. Observation plane is 50 mm above the MS. The simulated complexed E -field distributions under LHCP (xoz -plane) and RHCP (yoz -plane) illuminations are given in Figure 9b. The top, bottom, and internal views of the MS sample are given in Figure 9c–e, respectively. The near-field magnitudes under LHCP and RHCP wave illuminations at 27.38, 28.77, 29.69, and 30.62 GHz are given in **Figure 10a,b**, respectively. The power is focused on the predesigned positions under LHCP and RHCP illuminations. The measured intensity of other frequencies can be found in Videos SV3 and SV4 (Supporting Information).

5. Conclusion

Polarization-maintaining transmissive MSs have been demonstrated for spin-decoupled wavefront shaping. The meta-atom is built in a fashion of dual-polarized antennas on the top and bottom with phase delay lines connecting them. The dual-polarized

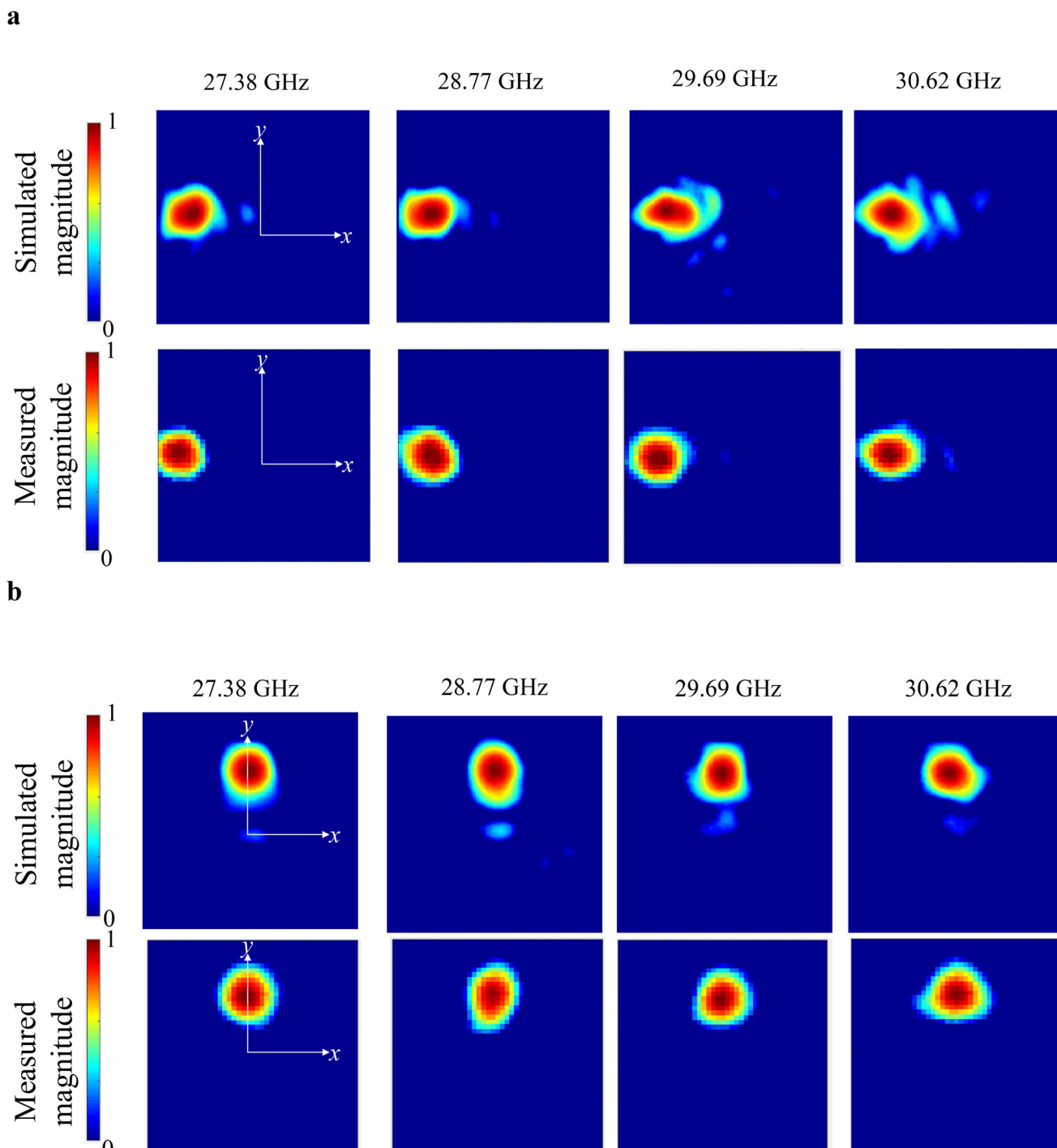


Figure 10. a) Simulated and measured co-polarization transmission magnitude under LHCP illumination. b) Simulated and measured co-polarization transmission magnitude under RHCP illumination.

antenna in the receiving side is fixed to receive the LHCP/RHCP incident waves. In contrast, the dual-polarized antenna on the transmitting side rotates, providing the opposite phase shift for the LHCP and RHCP. The absolute value of the phase shift is equal to the rotation angle. Meanwhile, adjusting the length of phase delay lines provides the same dynamic phases. Thus, the LHCP and RHCP wavefronts can be independently controlled,

while the polarization is not flipped after transmitting through the MS. Although spin-decoupled wavefront manipulations have extensively been studied, most previous works combine the P-B and dynamic phases. The P-B phase can only provide phase for the cross-polarized output fields without adding a phase to the co-polarized components. Therefore, the transmitted co-polarized components, LHCP incident to the LHCP output and RHCP

incident to the RHCP output, still cannot be decoupled by the P–B phase and dynamic phase schemes. Hence, the progress of the work lies in the polarization-maintaining phase modulate scheme, which can be regarded as a complementary approach for the P–B phase that only works in cross-CP components. Therefore, the underlying principle to achieve the polarization-maintaining principle differs from the strategy of adding a polarization conversion layer to traditional spin-decoupled MS. Though 64 different meta-atoms that are used to form the MS looks complicated, the meta-atom can actually be optimized with required performance rapidly by using the pattern-search-based algorithm. The multilayered configuration can be fast prototyped by multimaterial additive manufacturing. Two MSs with spin-decoupled polarization-maintaining functionalities are designed and experimentally verified.

Supporting Information

Supporting Information is available from the Wiley Online Library or from the author.

Acknowledgements

This was supported by Nano Dimension through collaborative projects. The authors would like to thank Omer Tangi, Joseph Samuya, Tomer Dahan, Dr. Jaim Nulman, and the technical support team at Nano Dimension (Israel, Hong Kong, and the USA) for the fabrication support. This work was supported by the Australian Research Council - ARC Linkage Projects (LP210300004) and ARC Linkage Infrastructure (LE220100035).

Open access publishing facilitated by University of Technology Sydney, as part of the Wiley - University of Technology Sydney agreement via the Council of Australian University Librarians.

Conflict of Interest

The authors declare no conflict of interest.

Data Availability Statement

The data that support the findings of this study are available from the corresponding author upon reasonable request.

Keywords

additive manufacturing, focusing, metasurfaces, orbital angular momentum, polarization maintaining, spin decoupling

Received: May 15, 2023
Published online: August 7, 2023

- [1] F. Aieta, M. Kats, P. Genevet, F. Capasso, *Science* **2015**, *347*, 1342.
[2] H. Wang, H. Ma, M. Chen, S. Sun, T. Cui, *Adv. Funct. Mater.* **2021**, *31*, 2100275.
[3] I. Kim, J. Jang, G. Kim, J. Lee, T. Badloe, J. Mun, J. Rho, *Nat. Commun.* **2021**, *12*, 3614.
[4] T. Cui, M. Qi, X. Wan, J. Zhao, Q. Cheng, *Light: Sci. Appl.* **2014**, *3*, e218.
[5] P. Georgi, Q. Wei, B. Sain, C. Schlickriede, Y. Wang, L. Huang, T. Zentgraf, *Sci. Adv.* **2021**, *7*, f9718.

- [6] Z. Jiang, D. Werner, *Adv. Funct. Mater.* **2014**, *24*, 7728.
[7] H. Zhang, X. Sha, Q. Chen, J. Cheng, Z. Ji, Q. Song, S. H. Yu, S. Xiao, *Adv. Mater.* **2022**, *34*, 2109255.
[8] J. Wang, J. Kühne, T. Karamanos, C. Rockstuhl, S. A. Maier, A. Tittl, *Adv. Funct. Mater.* **2021**, *31*, 2104652.
[9] M. Xu, Q. He, M. Pu, F. Zhang, L. Li, D. Sang, Y. Guo, R. Zhang, X. Li, X. Ma, X. Luo, *Adv. Mater.* **2022**, *34*, 2108709.
[10] K. Chen, Y. Feng, F. Monticone, J. Zhao, B. Zhu, T. Jiang, L. Zhang, Y. Kim, X. Ding, S. Zhang, A. Alù, C. Qiu, *Adv. Mater.* **2017**, *29*, 1606422.
[11] Z. Luo, M. Z. Chen, Z. X. Wang, L. Zhou, Y. B. Li, Q. Cheng, H. F. Ma, T. J. Cui, *Adv. Funct. Mater.* **2019**, *29*, 1906635.
[12] Q. Song, S. Khadir, D. Vézian, S. Chenot, V. Brandli Genevet, *Sci. Adv.* **2021**, *7*, eabe1112.
[13] J. Y. Dai, L. X. Yang, J. C. Ke, M. Z. Chen, W. K. Tang, X. Li, M. Chen, Z. H. Wu, Q. Cheng, S. Jin, T. J. Cui, *Laser Photonics Rev.* **2020**, *14*, 1900133.
[14] J. Zhu, Y. Yang, J. Lai, J. Nulman, *Adv. Opt. Mater.* **2022**, *10*, 2200928.
[15] X. Zang, B. Yao, L. Chen, J. Xie, X. Guo, A. V. Balakin, A. P. Shkurinov, S. Zhuang, *Light: Adv. Manuf.* **2021**, *2*, 10.
[16] Q. Song, X. Liu, C. Qiu, P. Genevet, *Appl. Phys. Rev.* **2022**, *9*, 011311.
[17] L. Q. Cong, N. N. Xu, J. G. Han, W. L. Zhang, R. Singh, *Adv. Mater.* **2015**, *27*, 6630.
[18] X. Ding, F. Monticone, K. Zhang, L. Zhang, D. Gao, S. N. Burokur, A. de Lustrac, Q. Wu, C. Qiu, A. Alù, *Adv. Mater.* **2015**, *27*, 1195.
[19] R. Xie, G. Zhai, X. Wang, D. Zhang, L. Si, H. Zhang, J. Ding, *Adv. Opt. Mater.* **2019**, *7*, 1900594.
[20] J. Zhu, S. Liao, Q. Xue, *IEEE Trans. Antennas Propag.* **2022**, *70*, 9357.
[21] H.-X. Xu, L. Han, Y. Li, Y. Sun, J. Zhao, S. Zhang, C.-W. Qiu, *ACS Photonics* **2019**, *6*, 211.
[22] C. Zheng, G. Wang, J. Li, J. Li, S. Wang, H. Zhao, M. Li, Z. Yue, Y. Zhang, Y. Zhang, J. Yao, *Adv. Opt. Mater.* **2021**, *9*, 2002007.
[23] Y. Xu, H. Zhang, Q. Li, X. Zhang, Q. Xu, W. Zhang, C. Hu, X. Zhang, J. Han, W. Zhang, *Nanophotonics* **2020**, *9*, 3393.
[24] G. Ding, K. Chen, G. Qian, J. Zhao, T. Jiang, Y. Feng, Z. Wang, *Adv. Opt. Mater.* **2020**, *8*, 2000342.
[25] J. Zhu, Y. Yang, F. Wang, J. Lai, M. Li, *Adv. Opt. Mater.* **2023**, *11*, 2202416.
[26] H.-X. Xu, G. Hu, M. Jiang, Y. W. S. Tang, Z. Wang, Y. Huang, X. Ling, H. Liu, J. Zhou, *Adv. Mater. Technol.* **2019**, *5*, 1900710.
[27] B. Yao, X. Zang, Y. Zhu, D. Yu, J. Xie, L. Chen, S. Han, Y. Zhu, S. Zhuang, *Photonics Res.* **2021**, *9*, 1019.
[28] Y. Xu, Q. Li, X. Zhang, M. Wei, Q. Xu, Q. Wang, H. Zhang, W. Zhang, C. Hu, Z. Zhang, *ACS Photonics* **2019**, *6*, 2933.
[29] P. Xu, L. Li, R. Li, H. Liu, *IEEE Trans. Antennas Propag.* **2021**, *69*, 7041.
[30] J. P. Balthasar Mueller, N. A. Rubin, R. C. Devlin, B. Groever, F. Capasso, *Phys. Rev. Lett.* **2017**, *118*, 113901.
[31] G. Ding, K. Chen, X. Luo, J. Zhao, T. Jiang, Y. Feng, *Phys. Rev. Appl.* **2019**, *11*, 044043.
[32] F. Ding, S. Tang, S. I. Bozhevolnyi, *Adv. Photonics Res.* **2021**, *2*, 2000173.
[33] H. Xu, C. Wang, G. Hu, Y. Wang, S. Tang, Y. Huang, X. Ling, W. Huang, C. Qiu, *Adv. Opt. Mater.* **2021**, *9*, 2100190.
[34] R. Jin, L. Tang, J. Li, J. Wang, Q. Wang, Y. Liu, Z.-G. Dong, *ACS Photonics* **2020**, *7*, 512.
[35] Z. Li, D. Zhang, J. Liu, J. Zhang, L. Shao, X. Wang, R. Jin, W. Zhu, *IEEE Trans. Antennas Propag.* **2022**, *70*, 378.
[36] Y. Guo, S. Zhang, M. Pu, Q. He, J. Jin, M. Xu, Y. Zhang, P. Gao, X. Luo, *Light: Sci. Appl.* **2021**, *10*, 63.
[37] Z. X. Wang, J. W. Wu, L. W. Wu, Y. Gou, H. F. Ma, Q. Cheng, T. J. Cui, *Adv. Opt. Mater.* **2021**, *9*, 2001609.
[38] X. Zang, B. Yao, Z. Li, Y. Zhu, J. Xie, L. Chen, A. V. Balakin, A. P. Shkurinov, Y. Zhu, S. Zhuang, *Nanophotonics* **2020**, *9*, 1501.

- [39] Y. Zhu, B. Lu, Z. Fan, F. Yue, X. Zang, A. V. Balakin, A. P. Shkurinov, Y. Zhu, S. Zhuang, *Photonics Res.* **2022**, *10*, 1517.
- [40] Y. Yuan, Q. Wu, S. N. Burokur, K. Zhang, *IEEE Trans. Microwave Theory Tech.* **2023**, 3256527.
- [41] Y. Yuan, K. Zhang, B. Ratni, Q. H. Song, X. M. Ding, Q. Wu, S. N. Burokur, P. Genevet, *Nat. Commun.* **2020**, *11*, 4186.
- [42] J. Zhu, Y. Yang, N. Hu, S. Liao, J. Nulman, *ACS Appl. Mater. Interfaces* **2021**, *13*, 59460.